

SUPPLEMENTARY MATERIAL

Apatite tracks melt evolution and metallogenic fertility in arc magmas

Chetan L. Nathwani^{1,2}, Matthew A. Loader², Jamie J. Wilkinson^{2,1}, Yannick Buret², Robert H. Sievwright², and Pete Hollings³

¹ Department of Earth Science and Engineering, Imperial College London, Exhibition Road, South Kensington Campus, London, SW7 2AZ, UK

² London Centre for Ore Deposits and Exploration (LODE), Department of Earth Sciences, Natural History Museum, Cromwell Road, South Kensington, London, SW7 5BD, UK

³Geology Department, Lakehead University, 955 Oliver Road, Thunder Bay, Ontario, P7B 5EL, Canada

Dataset DR1: Analyses of Durango apatite standard

2020086 Dataset DR1.xlsx

Dataset DR2: Whole-rock electron probe microanalysis and laser ablation–inductively coupled–mass spectrometry apatite data

2020086 Dataset DR2.xlsx

Supplementary Figures

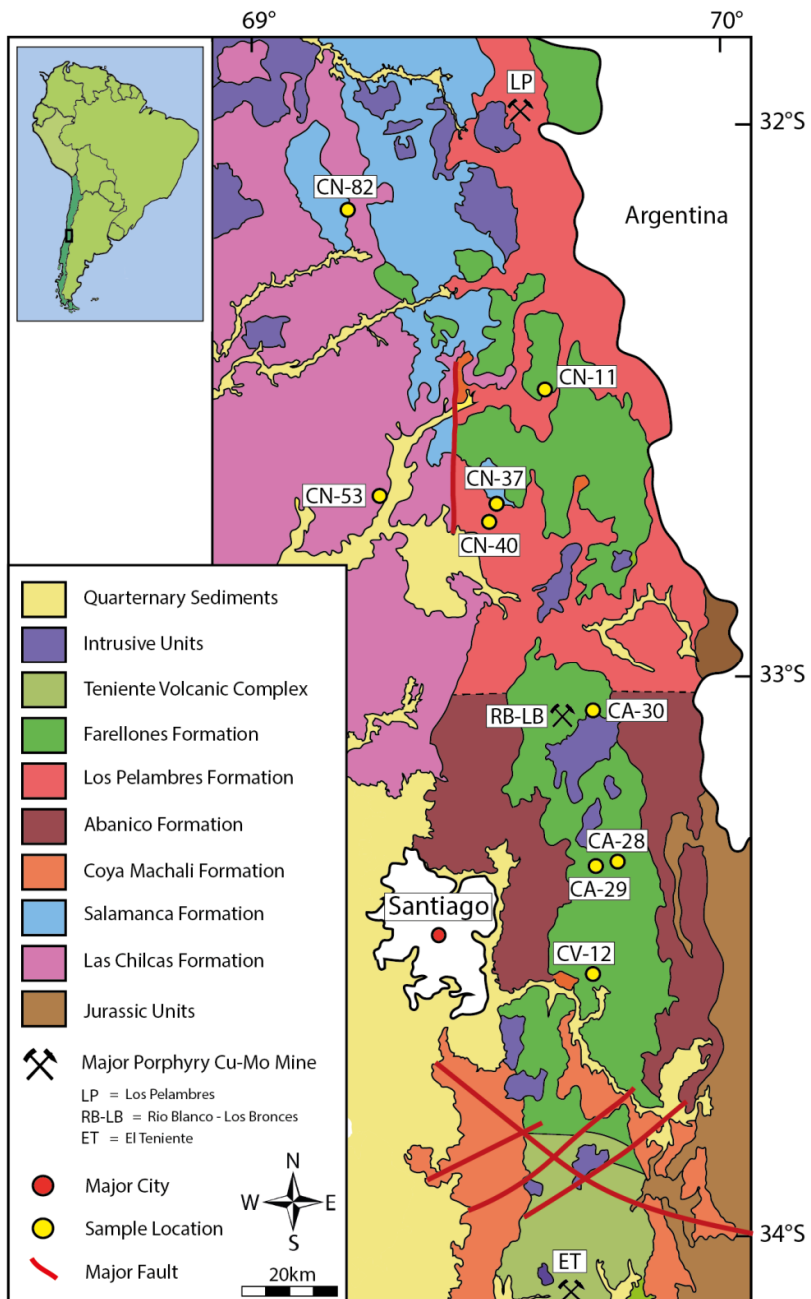


Figure S1. Regional geological map of the study area showing the locations of samples used in this study and the three major porphyry Cu-Mo deposits. After Hollings et al., (2005).

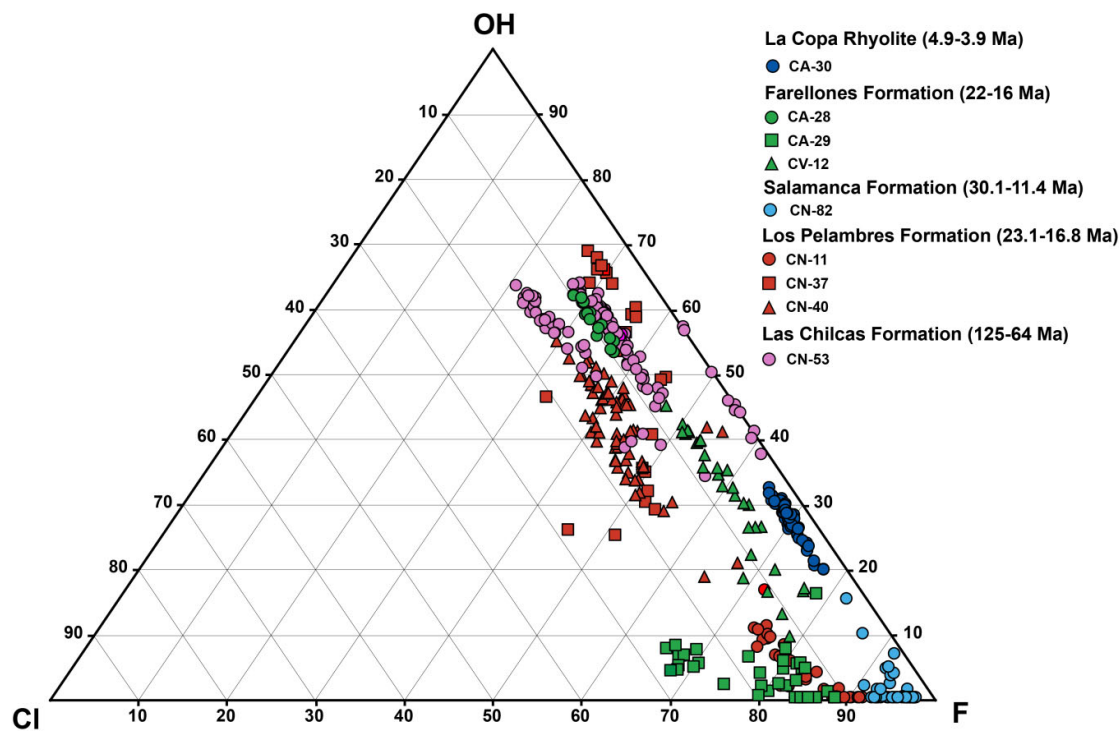


Figure S2. Ternary plot of OH, Cl and F wt % in apatite. Cl and F determined by microprobe; OH was estimated using stoichiometry on the basis of 16 cations in apatite.

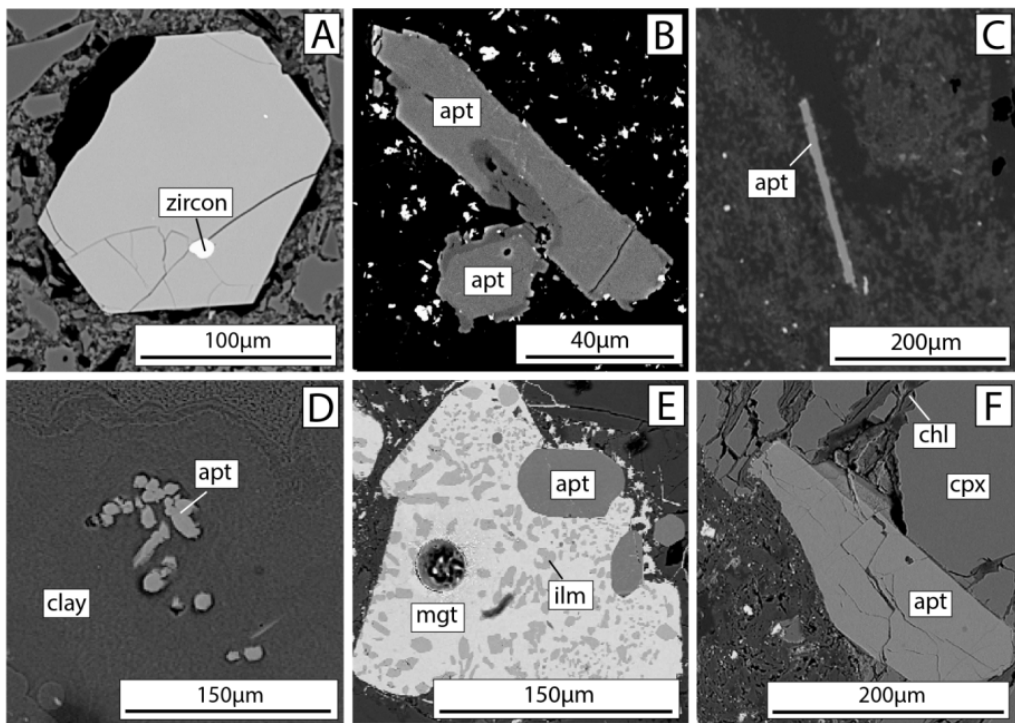


Figure S3. A selection of back-scattered electron images of apatite. (A) Euhedral apatite in CA-30 with zircon inclusion. (B) Apatite with alteration features with darkened rims/cores and sieving in CN-53. (C) Acicular apatite in the groundmass of CN-82. (D) Aggregates of apatite within clays replacing feldspars in CN-53. (E) Apatite hosted at rim of magnetite exsolving ilmenite. (F) Apatite hosted as an inclusion by clinopyroxene being altered to chlorite.

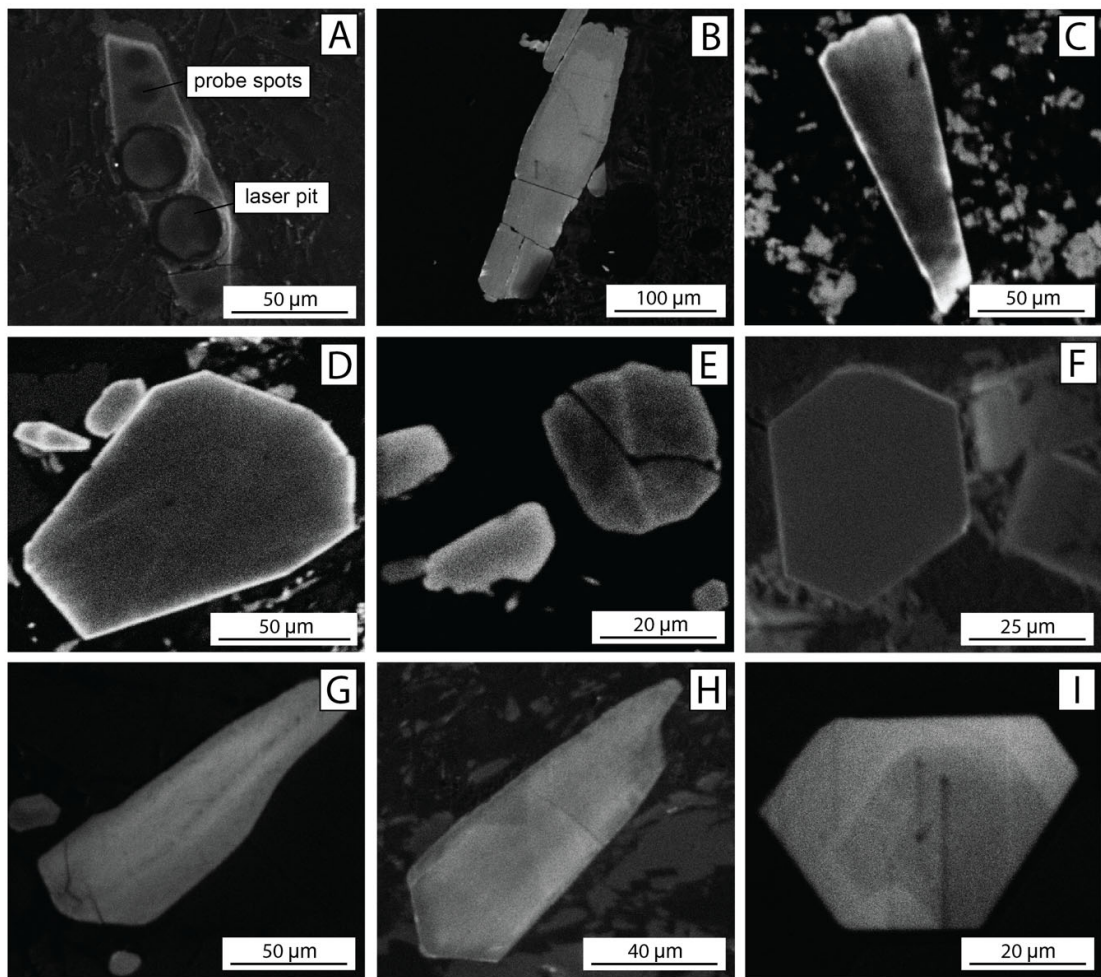


Figure S4: Scanning electron microscope cathodoluminescence images of apatite crystals in the samples analysed in this study. (A) Apatite crystal in CN-53. (B) Zoned apatite crystal in CN-11. (C) Apatite crystal in CN-37 with more luminescent rim. (D) Relatively homogeneous apatite crystals in CN-40. (E) Apatite crystals in CN-82 with one cracked crystal. (F) Relatively homogeneous apatite crystals in CA-28. (G) Zoned apatite crystal in CA-29. (H) Zoned apatite crystal in CV-12. (I) Zoned apatite crystal in CA-30.

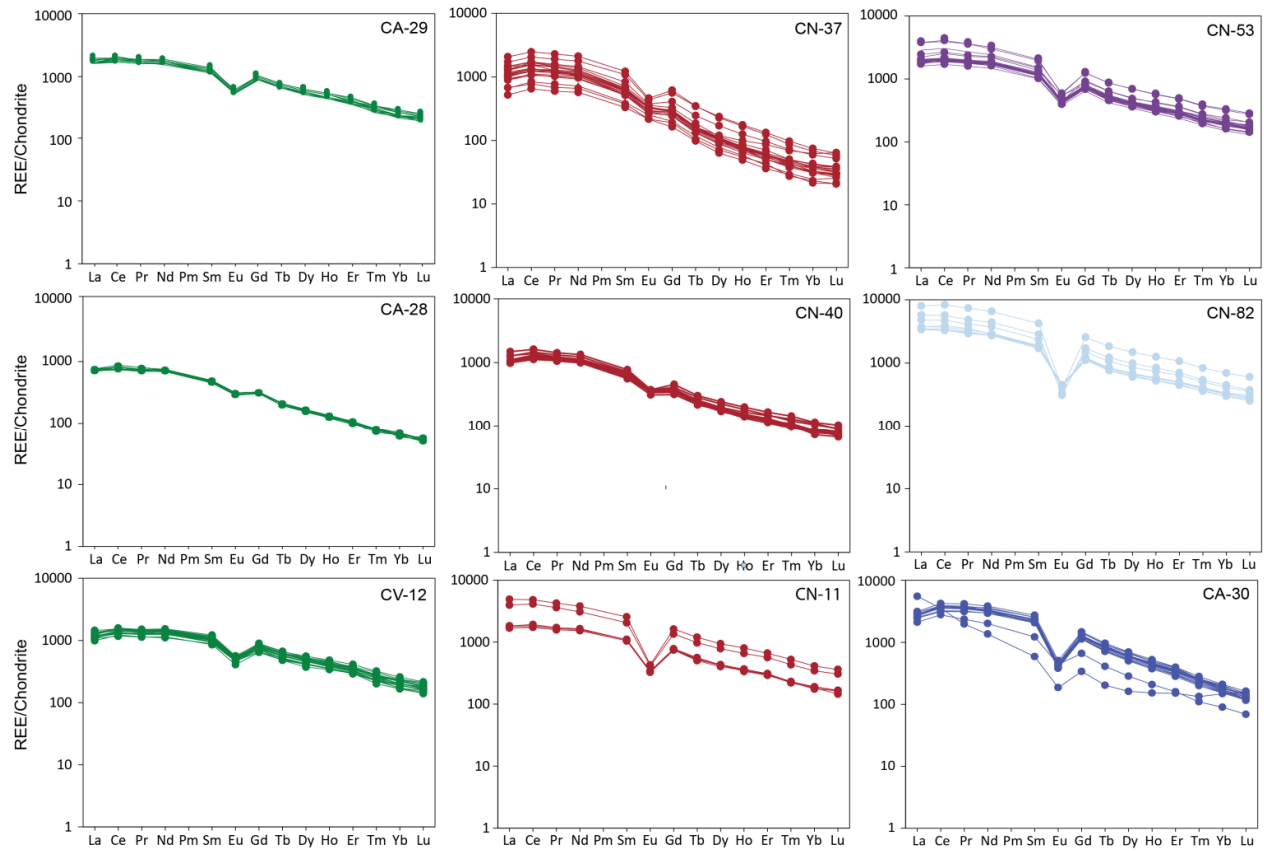


Figure S5. Chondrite-normalized (McDonough and Sun, 1995) REE plots for apatite crystals from the different formations sampled. Colors refer to host formation (legend as for Fig. S2).

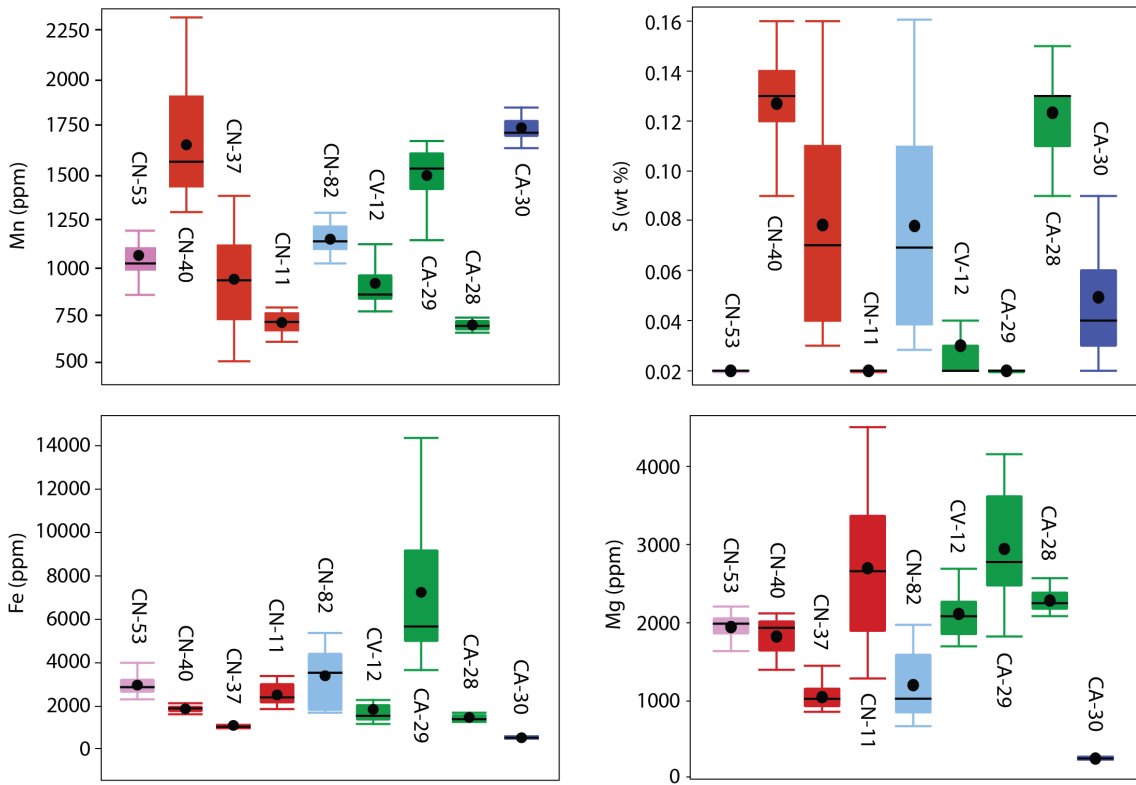


Figure S6. Box and whisker plots comparing a range of minor/trace elements in apatite between samples. Boxes show first to third quartile range with bars showing extremes of data (excluding any outliers). Line shows median value and dot shows mean value. Colors refer to host formation (legend as for Fig. S2).

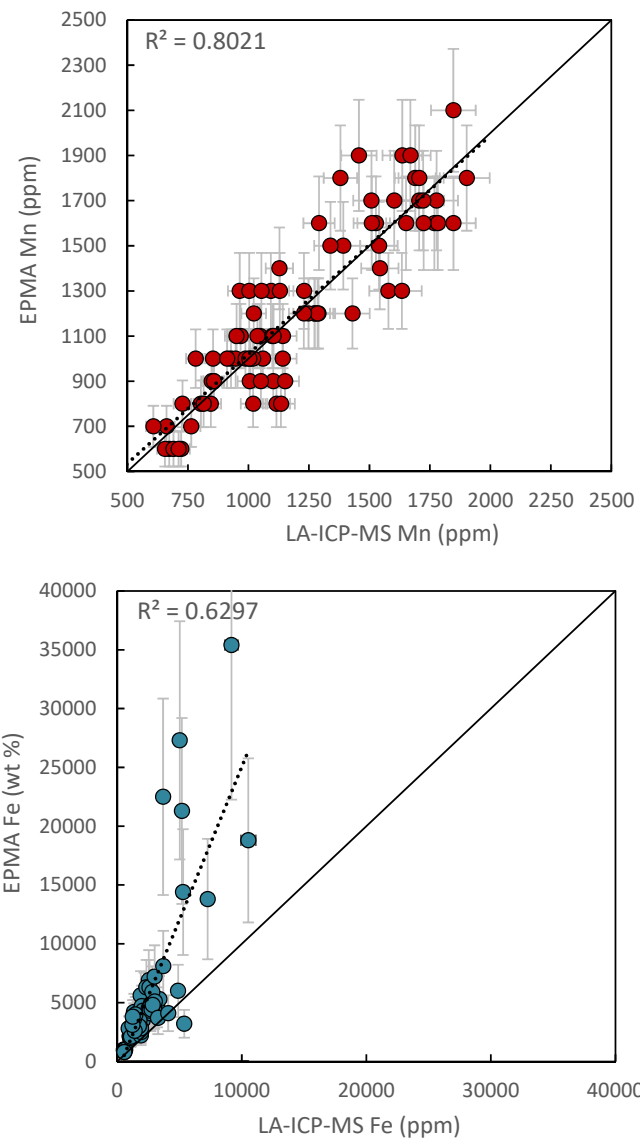


Figure S7. Apatite Mn and apatite Fe plots of EPMA vs. LA-ICP-MS data to assess data quality of LA-ICP-MS. Solid line shows 1:1 and dotted line shows line of best fit. Manganese shows good agreement by both methods whereas Fe shows some negative bias for LA-ICP-MS data in the best fit trend, and a few erroneously high EPMA values, likely due to argon hydroxide interference. Iron values determined by LA-ICP-MS are therefore not considered accurate and not used for further study.

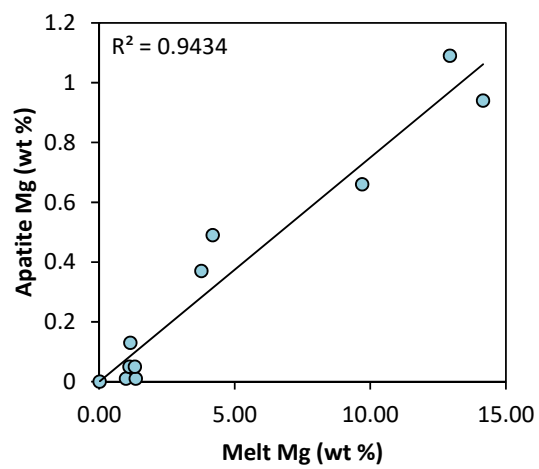


Figure S8. Apatite Mg vs. quenched melt Mg from the experimental study of Prowatke and Klemme (2006) demonstrating the ability for apatite to track melt differentiation.

Supplementary Data Tables

TABLE A1: SAMPLE INFORMATION (AGES AND SUMMARY OF MINERALOGY, ALTERATION AND APATITE SATURATION TEMPERATURES)

Sample	Formation	Age* (Ma)	WR SiO ₂ (wt%)	Mineralogy	Alteration (score)	AST† (°C)	No. Analyses (EMPA)	No. Analyses (LA-ICP-MS)
CN-53	Las Chilcas	125-64 ^[1]	65.56	plag/clay + qtz + cpx + mag + apt	clay + haem + rut (5/5)	1063	120	33
CN-82	Salamanca	30.1-11.4 ^[1]	70.88	plag + qtz + bt + mag + apt + zrc + ttn	qtz + haem (4/5)	903	50	17
CN-11	Los Pelambres	23.1-16.8 ^[5]	56.96	plag + cpx + amph + mag + apt	(2/5)	827	39	8
CN-37	Los Pelambres	21.9±2.2 ^[1]	63.18	plag/kfsp + amph + qtz + mag + apt + ttn	qtz + tit + alb (3/5)	905	31	29
CN-40	Los Pelambres	23.1-16.8 ^[5]	64.86	plag + amph + qtz + apt + zrc + ttn	chl + epd (4/5)	996	74	25
CV-12	Farellones	22-16 ^{[2][3]}	60.55	plag + kfsp + mag + amph + qtz + apt + ttn	calc + chl + epd (4/5)	944	43	34
CA-28	Farellones	22-16 ^{[2][3]}	63.55	plag + qtz + amph + mag + apt	haem (3/5)	986	19	14
CA-29	Farellones	22-16 ^{[2][3]}	56.77	plag + kfsp + cpx + mag + apt + ttn	alb + qtz (2/5)	906	40	17
CA-30	La Copa Rhyolite	ca. 4.5 ^[4]	70.78	qtz + plag + kfsp + bt + mag + apt + zrc	(1/5)	877	57	18

*Age source: ^[1] Hollings et al., (2005) ^[2] Deckart et al., 2010 ^[3] Piquer, (2017) ^[4] Toro et al., 2012 ^[5] Rivano et al., (1993)

† AST (Apatite saturation temperatures calculated using whole rock SiO₂ and P₂O₅ as an estimation of melt chemistry following the method of Piccoli & Candela, (2002) after Harrison and Watson, (1984).

Mineral abbreviations: plag = plagioclase, qtz = quartz, mag = magnetite, apt = apatite, bt = biotite, zrc = zircon, ttn = titanite, amph = amphibole, kfsp = alkali feldspar, haem = haematite, rut = rutile, alb = albite, chl = chlorite, epd = epidote

TABLE A2: ANALYTICAL QUALITY CONTROL OF LA-ICP-MS
DATA BASED ON 36 ANALYSES OF DURANGO APATITE
STANDARD

Element	Mean ¹	St. Dev ²	RSD ³	MDL ⁴
EMPA				
Ca	37.2	0.09	0.25	227
P	18.6	0.15	0.80	464
F	3.33	0.04	1.21	1026
Cl	0.34	0.02	5.94	399
Mn	0.01	0.01		
Si	0.17	0.00	0.00	179
S	0.11	0.009	8.51	160
Fe	0.03	0.009	37.1	232
Ce	0.85	0.28	3.30	936
LA-ICP-MS				
Li	3.2	0.35	10.91	0.606
Na	1851	47.18	2.55	15.5
Mg	206	3.95	1.92	0.37
Si	1254	99.31	7.92	120
P	159881	20024	12.52	8.8
V	29.7	0.54	1.82	0.03
Mn	93.5	2.02	2.16	0.26
Fe	292	16.72	5.71	3.64
Co	0.10	0.03	27.08	0.04
Cu	0.15	0.09	62.25	0.18
As	774	36.26	4.68	0.32
Rb	0.05	0.02	38.58	0.02
Sr	489	12.35	2.53	0.005
Y	428	11.73	2.74	0.002
Zr	0.37	0.03	7.27	0.005
Cd	0.19	0.09	44.64	0.03
Sn	1.8	0.42	23.50	0.53
Ba	1.5	0.14	9.11	0.02
La	3433	74.44	2.17	0.002
Ce	4486	102.98	2.30	0.005
Pr	346	8.22	2.37	0.001
Nd	1032	21.63	2.09	0.02
Sm	131	3.24	2.48	0.01
Eu	16	0.36	2.24	0.003
Gd	107	3.63	3.38	0.01
Tb	12	0.45	3.54	0.001
Dy	70	2.31	3.32	0.01
Ho	14	0.48	3.46	0.002

Er	37	1.26	3.42	0.01
Tm	5	0.17	3.66	0.001
Yb	27	0.87	3.21	0.01
Lu	3.63	0.13	3.68	0.001
Hf	0.02	0.01	40.84	0.01
Pb	0.44	0.04	9.32	0.04
Th	148.24	4.55	3.07	0.002
U	7.91	0.19	2.43	0.002

¹Mean value (wt % for EPMA, ppm for LA-ICP-MS)

²Standard deviation (wt % for EPMA, ppm for LA-ICP-MS)

³Relative standard deviation (%)

⁴Minimum detection limit (wt % for EPMA, ppm for LA-ICP-MS)

Analytical methods

All analysis performed in this study was carried out at the Imaging and Analysis Centre at the Natural History Museum in London.

Electron microprobe analysis (EMPA) was conducted using a Cameca SX100 electron microprobe with a 20 kV accelerating voltage and 20 nA beam current. In order to reduce the effects of anisotropic halogen diffusion in apatite along the c-axis when exposed to an electron beam, a count time of 60 s and a defocused beam diameter of 10 μm were used (Stormer et al., 1993). The following elements were analysed: P, Na, Ca, Cl, K, Mn, Fe, S, Sr, Si, Mg, F and Ce.

Trace element analysis was carried out using an ESI New Wave Research 193 nm excimer laser coupled to an Agilent 7700cs inductively-coupled-plasma mass spectrometer (ICP-MS). The laser was operated at 10 Hz, a fluence of 3.5 J cm^{-2} and a spot size of 20-50 μm . The background was analysed for 30 s followed by 60 s of ablation. The following isotopes were analysed: ^7Li , ^{23}Na , ^{24}Mg , ^{27}Al , ^{29}Si , ^{31}P , ^{39}K , ^{43}Ca , ^{45}Sc , ^{49}Ti , ^{51}V , ^{55}Mn , ^{57}Fe , ^{59}Co , ^{60}Ni , ^{63}Cu , ^{65}Cu , ^{66}Zn , ^{75}As , ^{85}Rb , ^{88}Sr , ^{89}Y , ^{90}Zr , ^{93}Nb , ^{95}Mo , ^{111}Cd , ^{118}Sn , ^{121}Sb , ^{137}Ba , ^{139}La , ^{140}Ce , ^{141}Pr , ^{145}Nd , ^{147}Sm , ^{151}Eu , ^{157}Gd , ^{159}Tb , ^{163}Dy , ^{165}Ho , ^{167}Er , ^{169}Tm , ^{173}Yb , ^{175}Lu , ^{177}Hf , ^{208}Pb , ^{209}Bi , ^{232}Th and ^{238}U . Data reduction was carried out using ExLAM 2000, selecting ablation intervals characterized by high and stable counts and removing instrumental spikes using an automated objective routine. NIST-612 glass and GSD-1G were used as the primary and secondary external standards and Ca was used as the internal standard. A Durango apatite standard was regularly analysed to ensure accuracy in the data and to confirm no effect of decreasing spot size on data quality.

Cathodoluminescence imaging of the apatites analysed in this study was carried out to identify any igneous (e.g. zoning) or hydrothermal features (e.g. alteration). This was completed after quantitative analysis in order to avoid any beam damage that influence EPMA analysis of halogens due to anisotropic halogen diffusion. Imaging was carried out using a Zeiss EVO 15LS scanning electron microscope (SEM) with a 10 kV accelerating voltage and a 3nA beam current. Imaging revealed zoning features and no unequivocal evidence for hydrothermal alteration (Figure S4).

Trace element fractionation model of apatite chemistry

Rayleigh fractionation model

The melt in equilibrium with apatite crystals was estimated using published mineral/melt partition coefficients using:

$$C_L = \frac{C_A}{D} \quad (\text{S1})$$

Where C_L is the liquid composition, C_A is the apatite composition and D is the partition coefficient. The trace element fractionation model calculates the chemistry of apatite and melts using Rayleigh fractionation:

$$C_L = C_0(F)^{D-1} \quad (\text{S2})$$

Where C_L is concentration of the element in the melt, C_0 is the element concentration in the initial melt, F is the melt fraction and D is the partition coefficient which in this model is a bulk partition coefficient (K_D).

Partition coefficients

Compositionally relevant partition coefficients were used from the literature: apatite (Prowatke and Klemme, 2006), plagioclase (Dunn and Sen, 1994), amphibole (Nandedkar et al., 2017), clinopyroxene (Blundy et al., 1998) and olivine (Dunn and Sen, 1994).

Table A3: Compilation of partition coefficients for mineral phases modelled

Mineral	Apatite	Amphibole	Clinopyroxene	Olivine	Plagioclase
Reference	Prowatke and Klemme, al., (2016) (2006)	Nandedkar et al., (2016)	Blundy et al., (1998)	Dunn and Sen, (1994)	Dunn and Sen, (1994)
Bulk composition	Basalt	Andesite	Basalt	Basalt	Basaltic-andeiste
T (°C)	1250	920	1255	Mineral/matrix	Mineral/matrix
P (MPa)	1000	700	1500	Mineral/matrix	Mineral/matrix
Mg	0.1*	19.63†	15.0†	42.0†	0.24†
Sr	1.37	0.339	0.062	0.018	Eq. S3
Y	2.91	3.145	1.27	0.033	0.038
Sm	5.68	2.115	0.67	0.028	0.083
Eu	Eq. S4	Eq. S4	Eq. S4	Eq. S4	Eq. S4
Gd	5.13	2.974	0.99	0.033	0.067

*Partitioning of Mg into apatite was not reported in experiments, $D_{\text{Mg(apatite)}}$ was estimated using reported partition coefficients for cations of equal charge and similar ionic radius. In support of our estimated value, at FMQ +2, in an augite minette starting composition, Righter et al., (2016) found $D_{\text{Mg(apatite)}} = 0.1$.

†Expressed as average wt % concentrations from EDS data

In plagioclase, $D_{\text{Sr(plag)}}$ and $D_{\text{Eu(plag)}}$ are largely dependent on temperature and feldspar composition (Blundy and Wood, 1991). Additionally, $D_{\text{Eu(plag)}}$ is controlled by fO_2 (e.g. Wilke and Behrens, 1999).

Accounting for variability in $D_{\text{Sr(plag)}}$ is necessary since its value will strongly influence modelled Sr/Y_{melt}. For each model, $D_{\text{Sr(plag)}}$ was therefore calculated following the experimental calibration of Blundy and Wood (1991)

$$D_{\text{Sr}} = e^{\frac{X_{\text{An}}(26800-26700)}{RT}} \quad (\text{S3})$$

Where X_{An} is the anorthite composition of the plagioclase (average value obtained from samples using SEM-EDS), R is the gas constant and T is temperature in Kelvin (900°C used based on approximate average of apatite saturation temperatures). The partition coefficient for $D_{\text{Eu(plag)}}$ is more complex as both Eu²⁺ and Eu³⁺ are incorporated into plagioclase (e.g. Wilke and Behrens, 1999, Aigner-Torres et al., 2007), and the partition coefficient for Eu ($D_{\text{Eu(min)}}$) into a mineral can be written as:

$$D_{\text{Eu(min)}} = \frac{D_{\text{Eu}^{3+}} + ((\frac{D_{\text{Eu}^{2+}}}{D_{\text{Eu}^{3+}}})_{\text{melt}} \times D_{\text{Eu}^{2+}})}{(\frac{D_{\text{Eu}^{2+}}}{D_{\text{Eu}^{3+}}})_{\text{melt}} + 1} \quad (\text{S4})$$

Where $D_{\text{Eu}^{2+}}$ is the partition coefficient of Eu²⁺ into the mineral and $D_{\text{Eu}^{3+}}$ is the partition coefficient of Eu³⁺ and $(\text{Eu}^{2+}/\text{Eu}^{3+})_{\text{melt}}$ is the ratio of Eu valence states in the melt. Using lattice-strain principles (Blundy and Wood, 1994), $D_{\text{Eu}^{2+}}$ can be approximated by D_{Sr} calculated by equation S3 (which additionally allows D_{Eu} to be calculated at X_{An} and T) and $D_{\text{Eu}^{3+}}$ can be approximated by interpolation of the partition coefficients of the neighbouring rare earths ($\sqrt{D_{\text{Sm}} \times D_{\text{Gd}}}$). The value of $(\text{Eu}^{2+}/\text{Eu}^{3+})_{\text{melt}}$ is dependent on temperature, fO₂ and melt composition. Experimental calibration gives the relationship of Eu valence in melts as (Burnham et al., 2015):

$$\frac{D_{\text{Eu}^{3+}}}{D_{\text{Eu}}} = \frac{1}{1 + 10^{-0.25 \log fO_2 - \frac{6410}{T} - 14.2\Lambda + 10.1}} \quad (\text{S5})$$

Where T is temperature in Kelvin and Λ is the optical basicity, where the average optical basicity of an arc magma is 0.55 (Tang et al., 2018). The value of $(\text{Eu}^{2+}/\text{Eu}^{3+})_{\text{melt}}$ was calculated for a fixed value for T and fO₂ of 900°C and FMQ +2 (e.g. Carmichael, 1991), based on apatite saturation temperatures and typical values for an intermediate arc magma. The Eu valence of a melt is nearly temperature independent (Fig. S9).

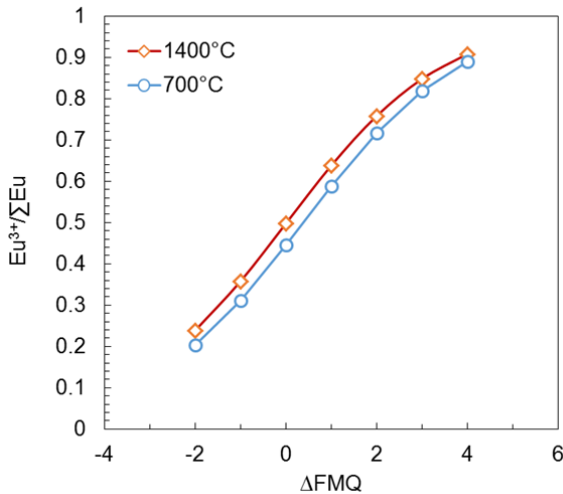


Figure S9. Oxygen fugacity dependence of Eu_{melt} calculated at 1400°C and 700°C for a melt with an optical basicity of 0.55 (Burnham et al., 2015). The two temperature curves demonstrate the near temperature independence of Eu valence in a melt.

Modelled conditions

Deep hydrous fractionation

We propose that this stage in the model is not recorded by apatite trace element chemistry in volcanic rocks. Under high pressure fractionation of a hydrous melt, apatite does not crystallize until temperatures $<860^{\circ}\text{C}$ (Nandedkar et al., 2014). Hence such a cryptic fractionation process could produce trends of increasing $\text{Sr}/\text{Y}_{\text{melt}}$ that are not recorded in our data. However, the high Sr/Y end product of such evolution could be inherited by apatite upon crystallization later in the magmatic differentiation process, likely in the shallow crust. This is akin to whole-rock chemistry responses to cryptic amphibole fractionation (e.g. Davidson et al., 2007, Smith et al., 2014). In order to explore the effect of deep crustal fractionation processes, we modelled a melt undergoing fractional crystallization (Fig. S10) using conditions typical of mid- to lower-crust conditions (1.0 GPa and 4.5 wt% H_2O ; Melekhova et al., 2014). This shows that our modelled starting compositions for shallow melt evolution based on the most primitive apatite in each trend (stars, Fig. S10) are consistent with prior deep crustal evolution. For the highest Sr/Y apatites in model B, the starting point does not depart from our modelled deep crustal evolution trend but this can be explained by onset of apatite crystallization after some increment of prior, shallow crustal crystallization.

Shallow crustal crystallization

In the second stage of our model, apatite is crystallized along the liquid line of descent of melts undergoing fractional crystallization of a shallow crustal assemblage. Starting melt compositions are estimated from back-calculating the melt from the most primitive apatite composition (i.e. apatite with highest Mg and/or Sr/Y). The crystallizing assemblage is that estimated from the phenocryst

assemblage of the host sample of the most primitive apatite composition. Apatites are crystallized at 10% fractional crystallization increments.

Modelling results

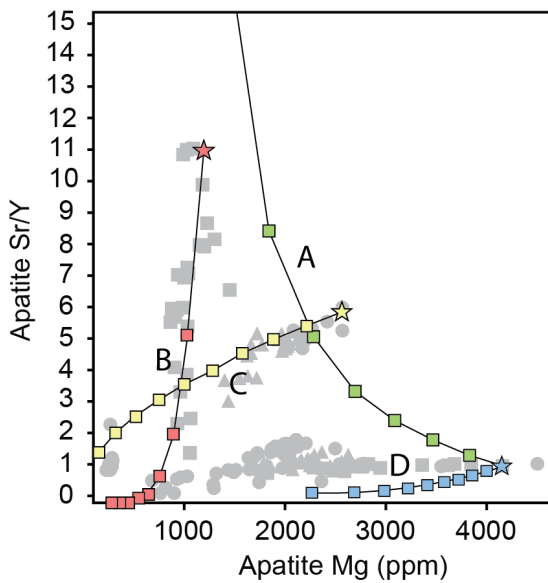


Figure S10. Summary diagram of the model results. Natural apatite data from the study is shown in gray. Stars represent starting compositions.

The tables below present results of modelling apatite trace element chemistry – showing apatite chemistry crystallized from melts undergoing the crystallization specific to the model.

TABLE S4: Model A

Melt fraction	Mg	Sm	Eu	Gd	Sr	Y	Sr/Y	Eu/Eu*
1.00	4500.00	185.00	32.00	189.00	611.00	673.00	0.91	0.52
0.90	4161.10	175.89	31.03	169.00	656.61	595.26	1.10	0.55
0.80	3812.36	166.24	29.97	149.13	711.63	518.94	1.37	0.58
0.70	3452.21	155.94	28.82	129.42	779.61	444.18	1.76	0.62
0.60	3078.54	144.84	27.55	109.88	866.20	371.16	2.33	0.67
0.50	2688.44	132.72	26.11	90.54	981.12	300.13	3.27	0.73
0.40	2277.62	119.27	24.46	71.44	1142.71	231.43	4.94	0.81
0.30	1839.22	103.91	22.48	52.63	1390.91	165.52	8.40	0.93
0.20	1360.73	85.57	19.95	34.22	1834.91	103.21	17.78	1.12
0.10	812.94	61.39	16.28	16.39	2946.42	46.03	64.01	1.56

TABLE S5: Model B

Melt fraction	Mg	Sm	Eu	Gd	Sr	Y	Sr/Y	Eu/Eu*
1.00	1250.00	61.00	14.60	41.19	887.00	80.00	11.09	0.89
0.90	1126.58	64.37	13.64	42.74	630.16	82.92	7.60	0.79
0.80	1002.99	68.36	12.63	44.55	430.00	86.32	4.98	0.70
0.70	879.18	73.19	11.59	46.69	278.81	90.33	3.09	0.60

0.60	755.14	79.18	10.49	49.29	169.07	95.20	1.78	0.51
0.50	630.81	86.90	9.32	52.56	93.57	101.30	0.92	0.42
0.40	506.16	97.39	8.06	56.85	45.36	109.30	0.42	0.33
0.30	381.08	112.80	6.69	62.90	17.84	120.55	0.15	0.24
0.20	255.43	138.75	5.14	72.54	4.79	138.41	0.03	0.16
0.10	128.90	197.67	3.28	92.55	0.50	175.26	0.00	0.07

TABLE S6: Model C

Melt fraction	Mg	Sm	Eu	Gd	Sr	Y	Sr/Y	Eu/Eu*
1.00	2700.00	70.74	17.76	58.80	530.00	100.00	5.30	0.84
0.90	2327.68	77.06	18.72	63.89	527.70	109.00	4.84	0.81
0.80	1971.90	84.79	19.86	70.10	525.14	120.02	4.38	0.79
0.70	1633.85	94.50	21.23	77.88	522.26	133.86	3.90	0.75
0.60	1315.02	107.10	22.94	87.94	518.95	151.85	3.42	0.72
0.50	1017.23	124.19	25.13	101.53	515.06	176.26	2.92	0.68
0.40	742.91	148.86	28.10	121.05	510.34	211.54	2.41	0.64
0.30	495.43	188.04	32.45	151.85	504.32	267.65	1.88	0.59
0.20	279.89	261.35	39.75	209.01	495.95	372.87	1.33	0.52
0.10	105.45	458.84	56.24	360.89	481.97	657.23	0.73	0.42

TABLE S7: Model D

Melt fraction	Mg	Sm	Eu	Gd	Sr	Y	Sr/Y	Eu/Eu*
1.00	4157.00	186.00	32.00	187.00	606.00	638.00	0.95	0.52
0.90	4034.90	204.10	33.13	205.13	560.05	701.84	0.80	0.49
0.80	3902.64	226.42	34.44	227.49	512.79	780.80	0.66	0.46
0.70	3757.94	254.69	35.99	255.80	464.02	881.11	0.53	0.43
0.60	3597.55	291.74	37.86	292.90	413.46	1013.05	0.41	0.39
0.50	3416.66	342.58	40.20	343.77	360.72	1194.82	0.30	0.36
0.40	3207.60	417.02	43.26	418.21	305.24	1462.24	0.21	0.32
0.30	2956.84	537.34	47.56	538.44	246.11	1897.18	0.13	0.27
0.20	2636.34	768.09	54.34	768.81	181.69	2738.42	0.07	0.22
0.10	2166.82	1414.71	68.27	1413.32	108.15	5128.39	0.02	0.15

TABLE A4. Mineral proportions and anorthite content of plagioclase used in the models. Sample shows the sample for which the X_{An} and assemblage is taken from (i.e. the host sample of the apatites that form the start of each trend).

Model	X_{An}	$D_{Eu(plag)}^2$	Sample	Assemblage crystallized
A ¹	N/A	N/A	N/A	Amphibole (66%), clinopyroxene (34%)
B	0.45	0.48	CN-37	Plagioclase (81%), amphibole (19%)
C	0.56	1.17	CN-40	Plagioclase (10%), clinopyroxene (25%)
D	0.62	1.00	CA-28	Plagioclase (30%), clinopyroxene (15%), olivine (5%)

¹Modelled assemblage from Melekhova et al., (2014) at 4.5 wt % H₂O and 1.0 GPa.

² $D_{Eu(plag)}$ calculated using Equation X

Estimating mineral proportions in samples

The modelling discussed previously requires an estimation of mineral proportions in samples. This was carried out using the image processing software ImageJ. Scans of samples were made using a Zeiss Axio Imager M1, which provides high resolution reflected, plane-polarised and cross-polarised images. Images were converted to 8-bit images and thresholds were used to isolate grayscale values for each phenocryst phase being estimated. Due to alteration, particularly in the case of plagioclase, this proved challenging due to the contrasting greyscale values of alteration products that have partially replaced phenocryst phases. Therefore, polygons were drawn around phenocryst phases to isolate their greyscale values (Fig. S11). Only phenocryst phases were used to estimate mineral proportions as assumed groundmass crystallization occurred late, after apatite crystallization. The percentage of each phenocryst present was then estimated using ImageJ's 'analyze % area' function and converted to proportions for use in the model.

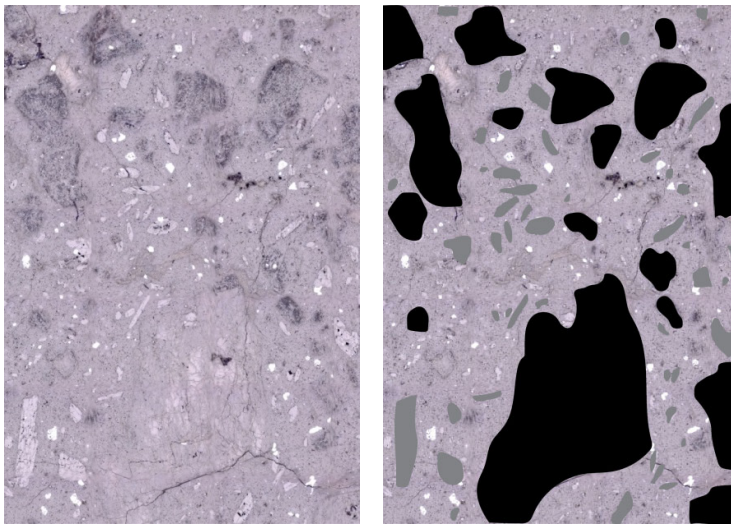


Figure S11. Reflected light image of CN-37 and polygons drawn to estimate mineral proportions.
Black = plagioclase feldspar, grey = amphibole.

Model – sensitivity of partition coefficients

The partitioning of trace elements is partly dependent on the composition and temperature of the melt. It therefore may be possible that trends observed in this study could reflect melt composition and temperature. For example, $D_{\text{Sr}}(\text{apatite/melt})$ increases 1.1 (at approximately 40 wt % SiO_2) to 5.10 in more felsic melts ($\text{SiO}_2 > 60$ wt %). However, since we have used trace element ratios, and it is expected that the change will occur both for the denominator and numerator in the ratio (e.g. for both D_{Sr} and D_Y), we expect the effect of melt composition can be negated. Experimental studies show no systematic change in D_{Sr}/D_Y for apatite (Fig. S12). The same may be true for the effect of temperature and pressure on apatite trace element partitioning. However, it is known that temperature changes may fractionate different valence states during trace element partitioning (e.g. Blundy and Wood 2003). It is difficult to directly assess the effect of temperature on

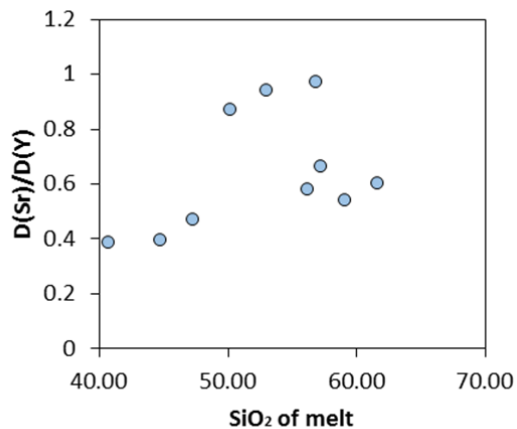


Figure S12. A plot of apatite D_{Sr}/D_Y with variable SiO_2 of the quenched melt from the experimental study of Prowatke and Klemme (2006).

Figure S13. A and B. Deep fractionation crystallization models run at high and low SiO_2 . C and D. Shallow fractional crystallization models run at high and low SiO_2 . For the blue model, the difference between high and low SiO_2 models was not discernible. Colors are same as used in figure in text.

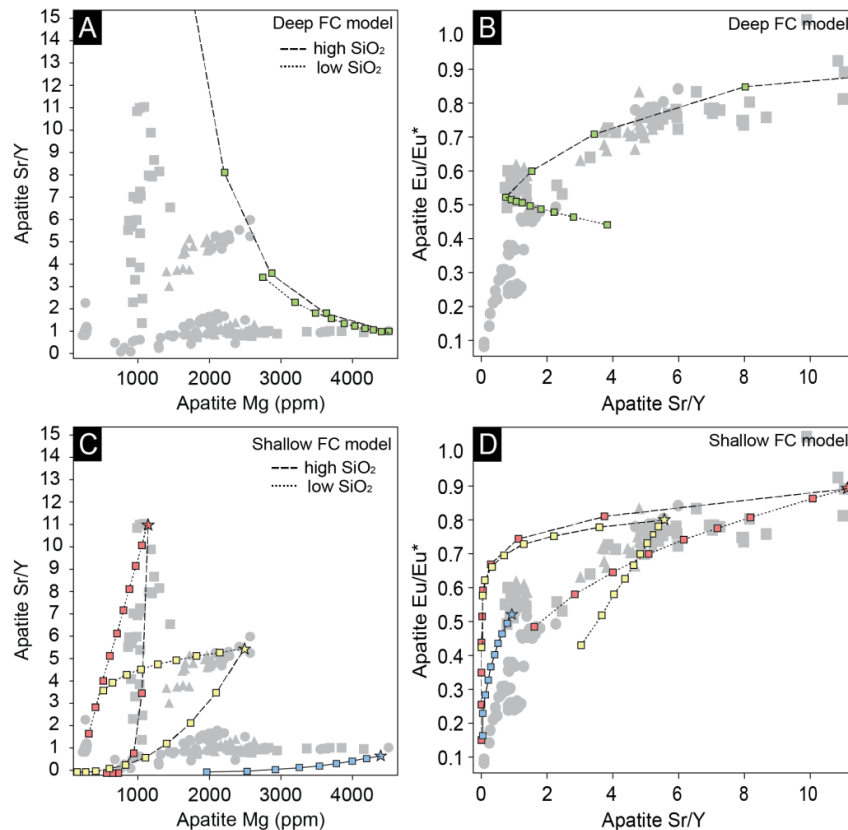


Figure S13. A and B. Deep fractionation crystallization models run at high and low SiO_2 . C and D. Shallow fractional crystallization models run at high and low SiO_2 . For the blue model, the difference between high and low SiO_2 models was not discernible. Colors are same as used in figure in text.

fractionating valence states in apatite since no apatite experimental studies to our knowledge are performed under polythermic conditions. Therefore our model assumes no valence fractionation during apatite-melt partitioning.

We further assessed the sensitivity of our model to changes in partition coefficients by running two extreme models – one at high SiO₂ and one at low SiO₂ using different partition coefficients in the literature and by varying temperature and plagioclase anorthite content for the plagioclase theoretically determined partition coefficients (Fig. S13). We find that the rate of increase in Sr/Y_{melt} in the deep FC model is strongly dependent on SiO₂ since Y is strongly compatible in amphibole at high SiO₂ (Nandedkar et al. 2016). We also find decrease in Sr/Y_{apatite} is strongly related to the anorthite content of plagioclase crystallized, since D_{Sr} increases for plagioclase with decrease anorthite content. In spite of this, we do not find that altering partition coefficients has a strong effect on the trends we model.

Table A5: Partition coefficients used in the apatite sensitivity analysis, using values found in experimental studies of mafic (low SiO₂) and felsic (high SiO₂) compositions.

Model	Apatite		Amphibole		Clinopyroxene		Plagioclase	
	Low SiO ₂	High SiO ₂						
Sm	4.99	16.10	0.85	5.45	0.38	5.50	-	-
Eu¹	3.66	11.65	1.09	5.92	0.35	3.84	0.35	3.95
Gd	4.65	13.90	1.19	7.85	0.58	5.50	-	-
Sr¹	1.1	4.30	0.42	0.57	0.08	0.17	1.28	12.6
Y	2.8	7.10	1.28	9.74	0.52	5.50	-	-

¹Sr and Eu partition coefficients were determined theoretically, using X_{An} = 0.9 and T = 1100°C for low SiO₂ and using X_{An} = 0.1 and T = 800°C for high SiO₂

Apatite literature data

In order to assess the wider applicability of the tool generated in our study we considered pre-existing, albeit limited, datasets. We find that data from ore-associated intrusive rocks in south-west China (Pan et al., 2016) and El Salvador porphyry Cu deposit in Northern Chile (unpub. Lee PhD Thesis, 2008) show near identical trends in Sr/Y and Eu/Eu* to results presented in this study. As noted by Pan et al., (2016), the porphyry Cu-associated intrusives (Pulang and Tongchanggou), which have adakite-like whole-rock chemistry, have higher apatite Sr/Y and Eu/Eu* than non-adakite-like from the same area (Xiuwacu). Apatite retained this chemical signature, in contrast to whole-rock chemistry, in more altered samples. At El Salvador, the syn-mineralization K and L porphyries have modest Sr/Y and Eu/Eu* whereas the late latite dykes possess a significantly elevated apatite Sr/Y and Eu/Eu*. This is consistent with apatite that crystallized during shallow crustal melt evolution from a

melt that had highly fractionated in the deep crust, as expected for magmas parental to porphyry Cu deposits. Unfortunately, neither datasets report Mg in apatite.

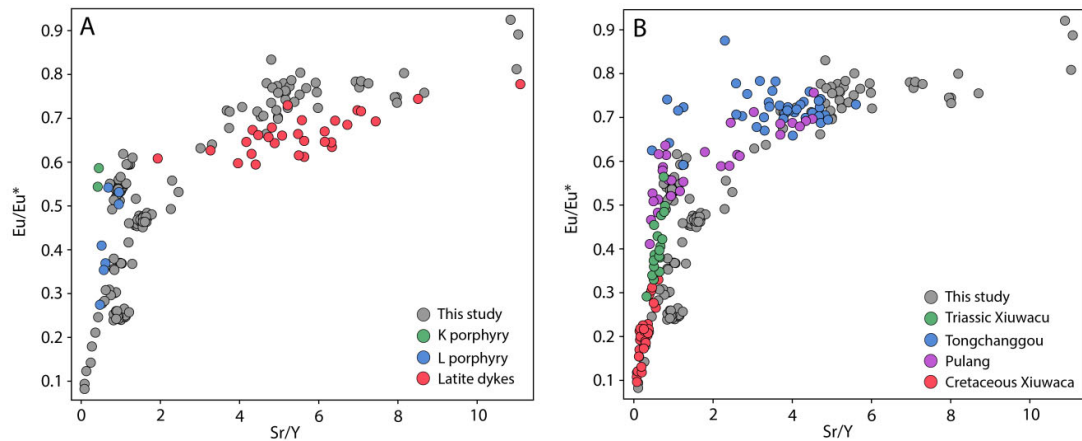


Figure S14. Apatite Eu/Eu* vs. apatite Sr/Y in (A) intrusive rocks at El Salvador porphyry Cu deposit in Northern Chile (unpub. Lee PhD Thesis 2008) and (B) ore-associated intrusives in south-west China (Pan et al., 2016).

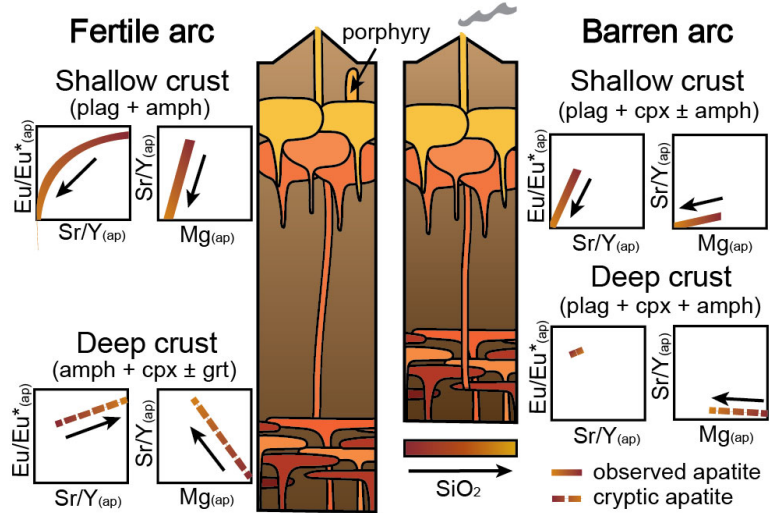
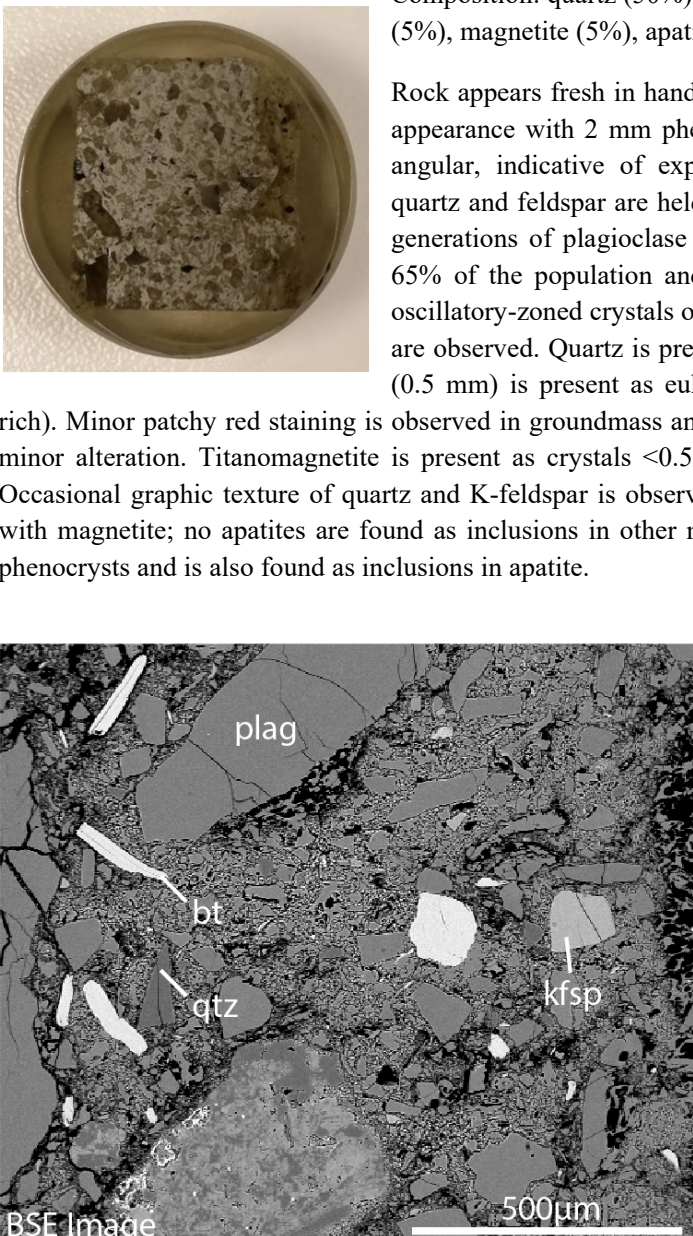
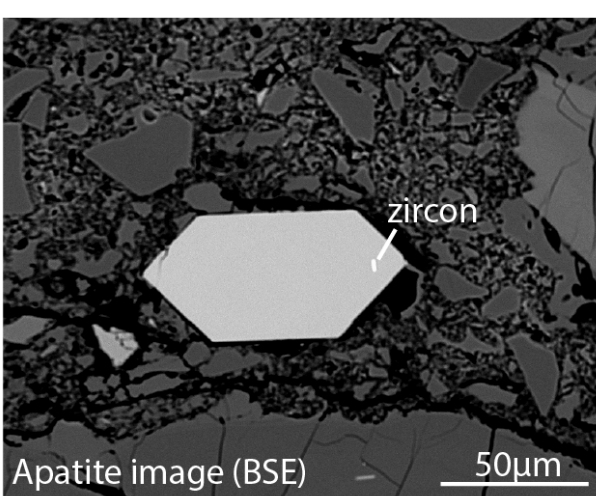
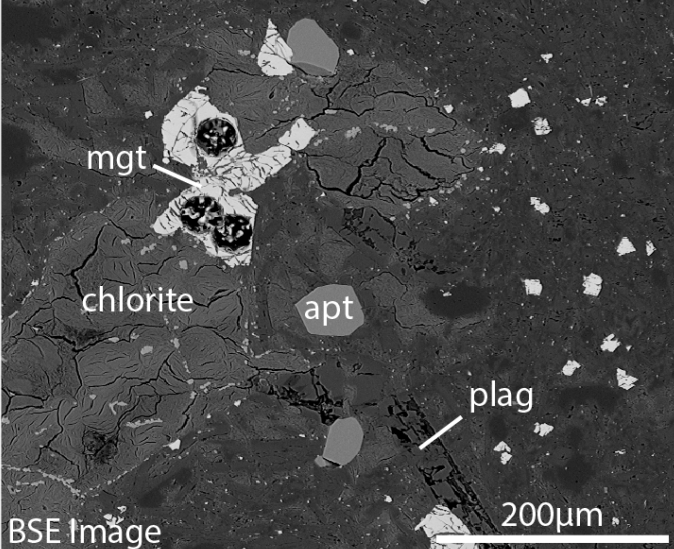
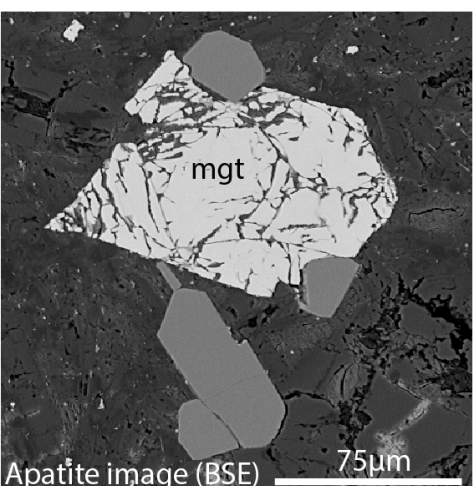
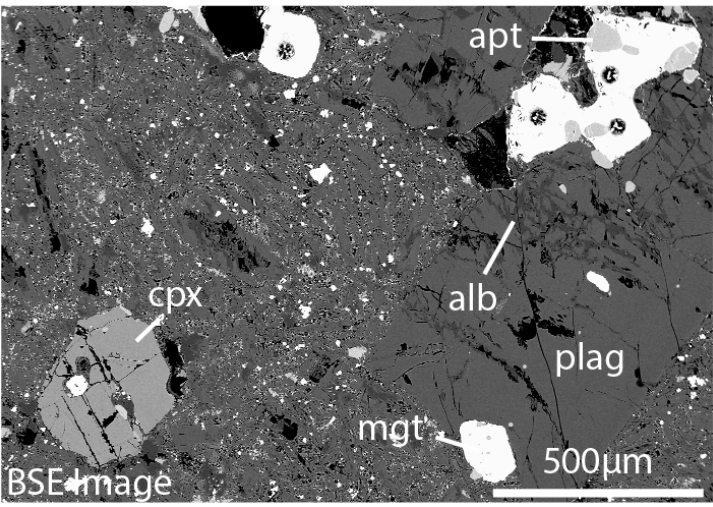
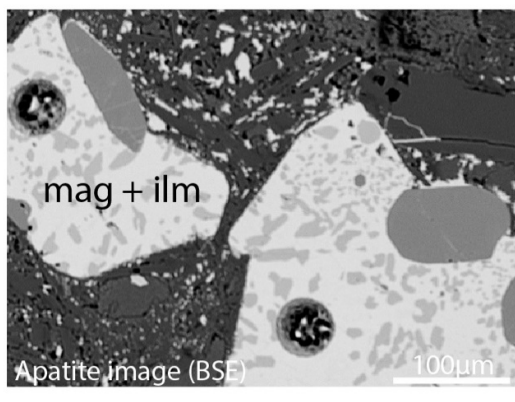


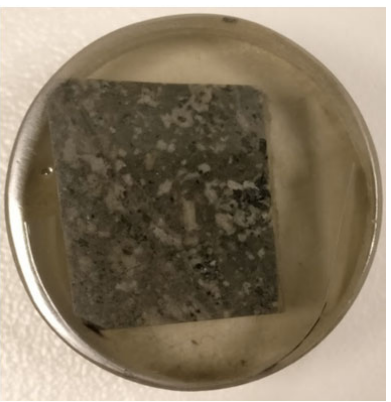
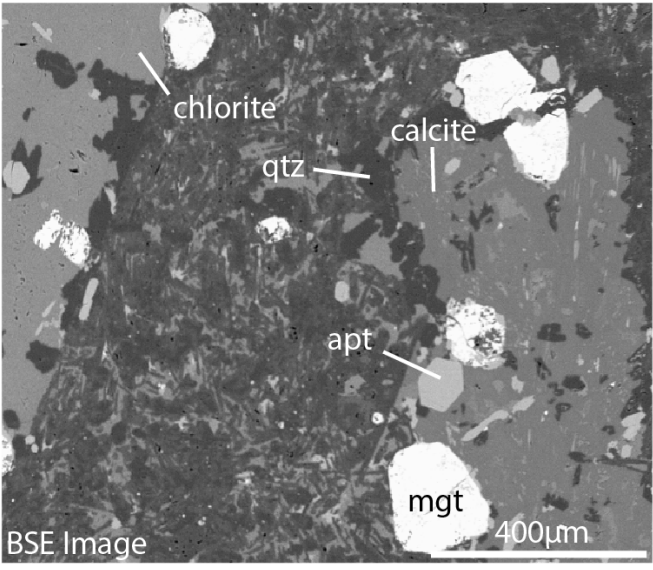
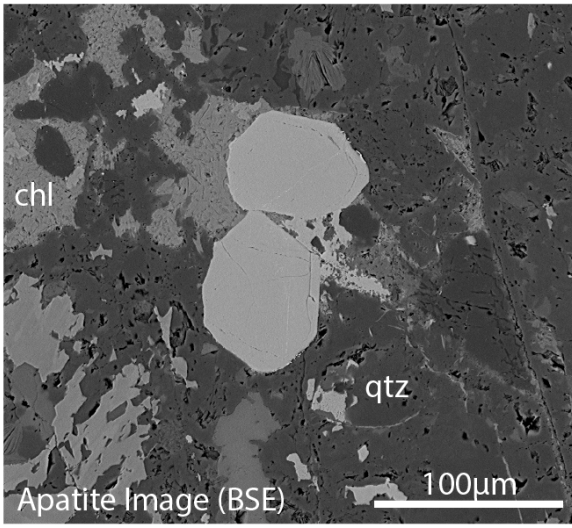
Figure S14. Schematic illustration of the model for apatite chemistry evolution in Central Chilean volcanics in: (A) thick crust where magmas undergo extensive deep crustal fractionation (a metallogenically fertile arc segment); and (B) thinner crust where deep crustal fractionation is limited (a metallogenically barren arc segment). Dashed lines on plots illustrate “cryptic” apatite chemistry – i.e. apatite chemistry that would be produced if crystallized in the deep crust – and solid lines illustrate observed apatite compositions.

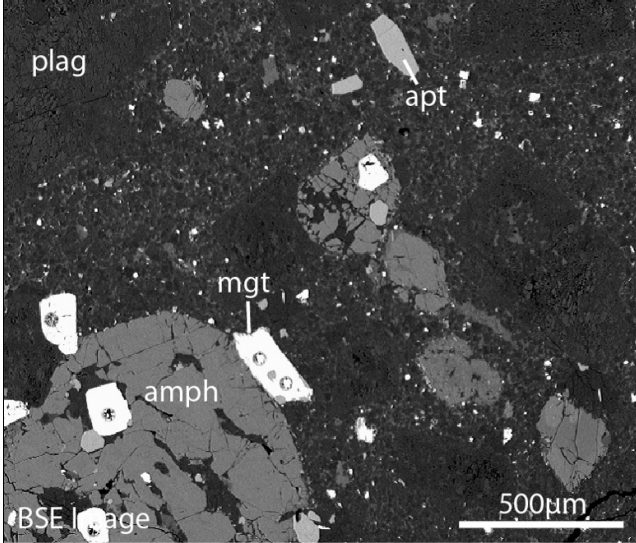
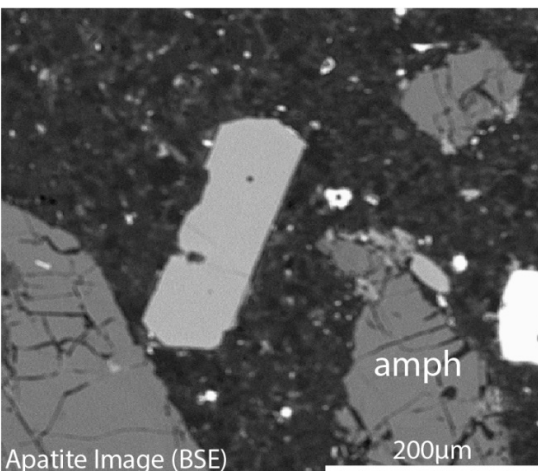
Rock Descriptions

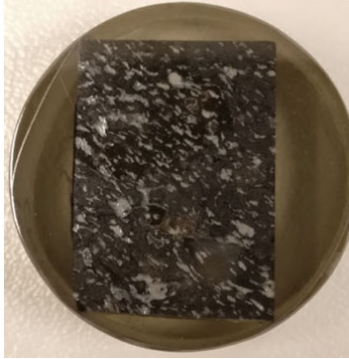
CA30	La Copa Rhyolite	SiO_2 (wt %) = 70.8%	GPS coordinates = 355172, 6380382
	<p>Composition: quartz (50%), plagioclase feldspar (30%), K-feldspar (10%), biotite (5%), magnetite (5%), apatite and zircon.</p> <p>Rock appears fresh in hand specimen with leucocratic, ignimbritic and porphyritic appearance with 2 mm phenocrysts (60%) in an ashy matrix (40%). Crystals are angular, indicative of explosive emplacement. In thin section, phenocrysts of quartz and feldspar are held within a fine, glassy, opaque matrix. Two contrasting generations of plagioclase feldspar are evident, with unzoned antecrysts forming 65% of the population and which in some cases form glomerocrysts. Younger, oscillatory-zoned crystals of plagioclase are also present (35%). K-feldspar crystals are observed. Quartz is present as anhedral phenocrysts up to 4 mm in size. Biotite (0.5 mm) is present as euhedral platy crystals with very strong body color (Fe-rich). Minor patchy red staining is observed in groundmass and in some cases surrounding feldspar grains, indicating minor alteration. Titanomagnetite is present as crystals <0.5 mm in size, usually with apatite present at the rims. Occasional graphic texture of quartz and K-feldspar is observed. Apatite is found in the groundmass and associated with magnetite; no apatites are found as inclusions in other mineral phases. Zircon is a fairly common inclusion in phenocrysts and is also found as inclusions in apatite.</p>  		

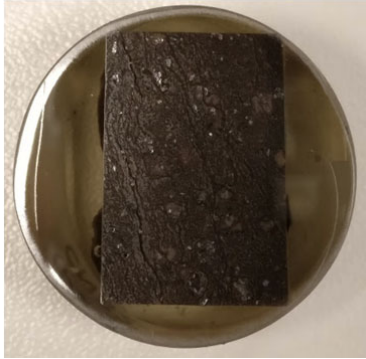
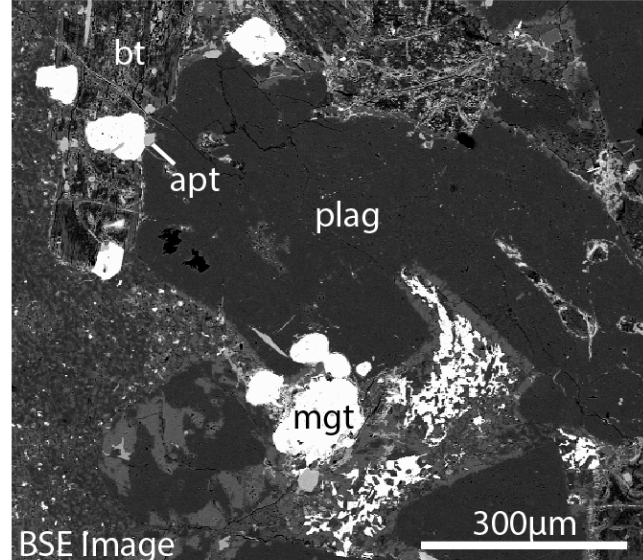
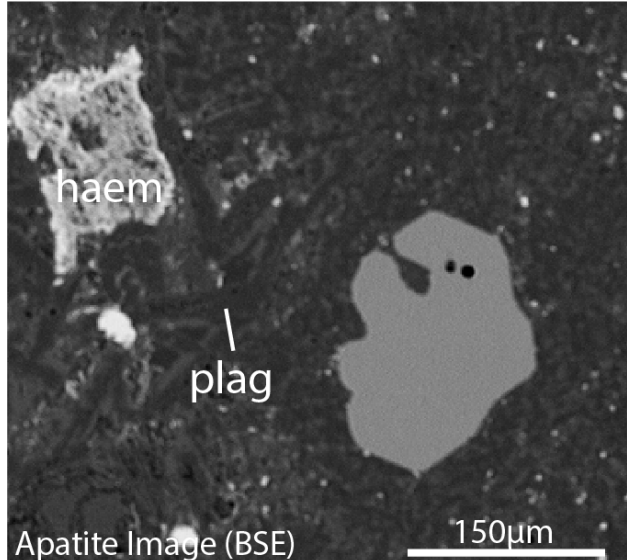
CA28	Farellones	SiO_2 (wt %) = 63.6%	GPS coordinates = 382881, 6308109
		<p>Composition: Plagioclase (55% - 30% phenocrysts, 25% groundmass), olivine (10%), chlorite + epidote (25%), magnetite (10%), apatite.</p>	
		<p>In hand specimen, the rock is melanocratic with porphyritic texture (feldspar phenocrysts visible). Mafic phenocrysts are present with strong yellow body color with stubby rectangular sections (clinopyroxene?). These have usually been pseudomorphed by chlorite but are recognisable by habit. Plagioclase feldspar phenocrysts are also present. Olivine phenocrysts present up to 0.5 mm in size. Euhedral magnetite (0.5 mm) and quartz (0.2 mm) crystals are also present. The sample's groundmass consists of microlitic sub-trachytic feldspar, magnetite and glass. Apatite is typically found in the groundmass in association with magnetite and as mineral inclusions. Plagioclase appears strongly altered to an iron-rich alteration product; feldspars were found to contain ~0.5 wt % FeO. Chlorite and epidote (propylitic</p>	
		 <p>BSE Image</p> <p>mgt chlorite apt plag 200μm</p>	 <p>mgt Apatite image (BSE) 75μm</p> <p>alteration) are also visible in veinlets.</p>

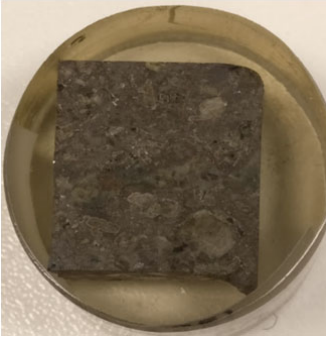
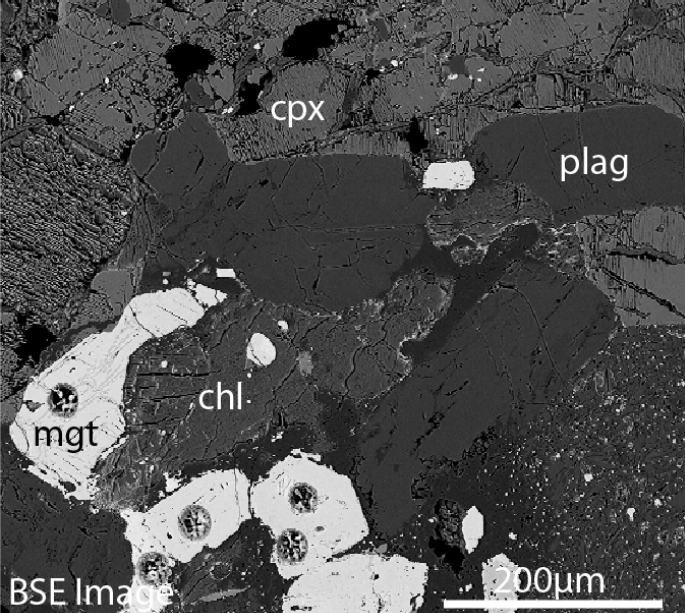
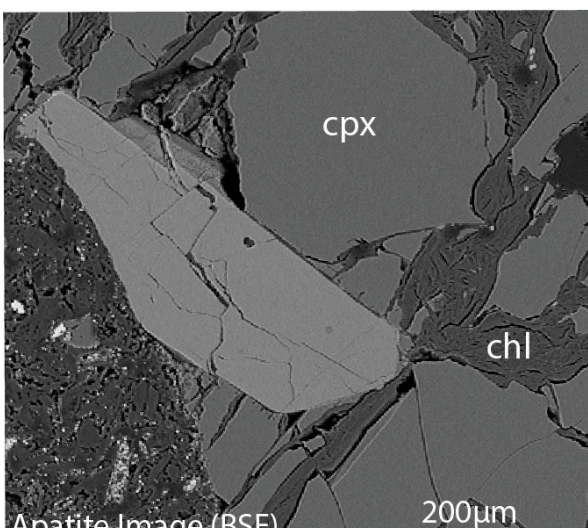
CA29	Farellones	SiO_2 (wt %) = 56.8%	GPS coordinates = 378555, 6307593
	<p>Composition: plagioclase feldspar (65%), K-feldspar (15%), clinopyroxene (10%), magnetite (10%), apatite, titanite.</p> <p>Porphyritic andesite containing phenocrysts of predominantly plagioclase (up to 3 mm) and clinopyroxene (up to 0.3 mm) in a matrix of plagioclase and oxides. Plagioclase phenocrysts larger than 1 mm are homogeneous whilst those which are around 400-750 microns in size often have sodic cores and are oscillatory zoned. Feldspar laths are partially aligned into a sub-trachytic texture. Minor K-feldspar is present comprising 20% of the feldspars. Clinopyroxene is present as euhedral phenocrysts. Magnetite is a common accessory mineral in the groundmass (often interstitial between finer plagioclase laths and as subhedral-anhedral grains less than 100 microns) and as euhedral-subhedral crystals in phenocrysts (up to 500 microns). Magnetite often contains globular-vermicular ilmenite. Sub- to euhedral apatite is present most commonly at the margins of magnetite crystals with some as large as 75 microns. Titanite is present as subhedral crystals less than 50 microns in size. Alteration is present in the sample as albitisation of feldspars with veins of albite and quartz.</p>		
	 		

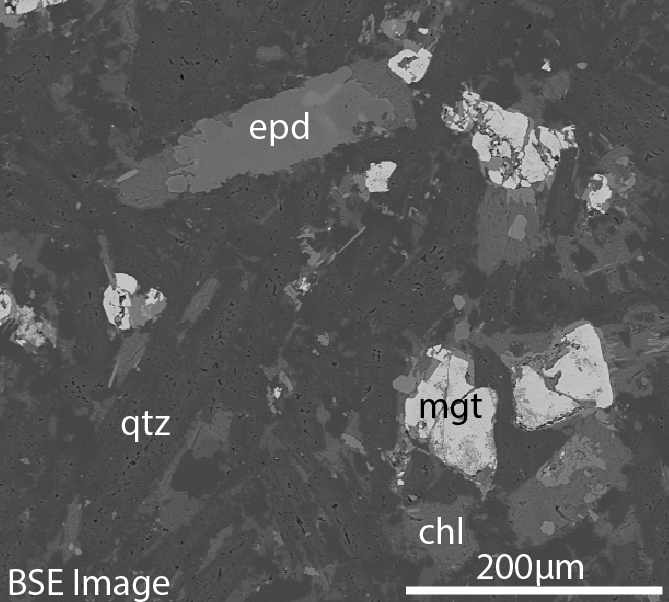
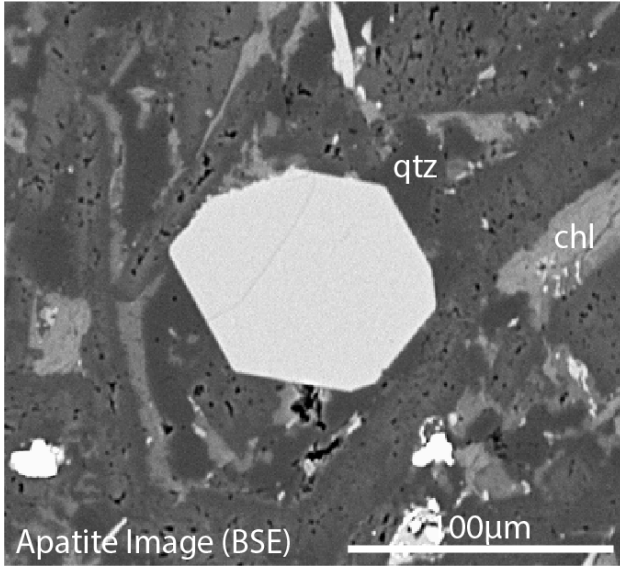
CV12	Farellones	SiO_2 (wt %) = 60.6%	GPS coordinates = 375953, 6284829
	 <p>Composition: plagioclase feldspar (45%), K-feldspar (10%), magnetite (10%), chlorite + epidote (15%), calcite (15%), quartz (5%), apatite, titanite.</p> <p>Porphyritic andesite containing plagioclase phenocrysts (1 mm). Plagioclase feldspar is strongly altered and in most cases has been pseudomorphed by calcite, chlorite, epidote and quartz. Epidote alteration is patchy and is seen mantling, or in some cases at the cores of, plagioclase, as well as in the groundmass. Chlorite and epidote have replaced clinopyroxene with some clinopyroxene remaining. Magnetite up to 0.5 mm in size is common, often as inclusions at the margins of plagioclase crystals. Magnetite crystals are fractured and mottled, having likely undergone hydrothermal alteration. Matrix consists of microphenocrysts of plagioclase and minor K-feldspar (<100 microns) with quartz and amphibole. Apatite is found infrequently associated with magnetite as euhedral crystals and also in patches of matrix as euhedral crystals. Apatite at the margins of pseudomorphed feldspar crystals is present. The sample is very strongly propylitically altered. However, despite the strong alteration overprint, apatites appear fresh and up to 100 microns in size (basal section). Titanite is observed as anhedral, mottled crystals.</p>  		

CN37	Los Pelambres	SiO_2 (wt %) = 63.2%	GPS coordinates = 355172, 6380382
		<p>Composition: plagioclase (60%), amphibole (15%), quartz (10%), magnetite (10%), alkali feldspar (5%), apatite, titanite.</p> <p>Porphyritic rock containing phenocrysts of feldspar (both plagioclase and K-feldspar) and amphibole. Amphibole phenocrysts are up to 3 mm in size, but are typically 1-2mm. They contain up to 7 wt % calcium. Feldspar phenocrysts, up to 0.5 cm in size, are usually extremely weathered. Feldspars have likely undergone some sub-solidus alteration. Groundmass consists of microlitic plagioclase and potassium feldspar with interstitial quartz. Magnetite is often fractured and found as crystals up to 500 microns but is also interspersed in the groundmass. Magnetite is commonly rimmed by titanite, indicative of hydrothermal alteration. Titanite is also present as subhedral crystals around 50 microns in size in the groundmass. Apatite is present but is not as common as in other samples. It occurs as euhedral crystals up to 150 microns. In one case it appears embayed, likely due to melt resorption. Quartz veining present in sample.</p>	
			 <p>Apatite Image (BSE)</p> <p>200μm</p>

CN53	Las Chilcas	SiO_2 (wt %) = 65.6%	GPS coordinates = 332694, 6382660
	<p>Composition: feldspars and clays (70%), quartz (10%), pyroxene (10%), magnetite (10%), apatite, rutile.</p> <p>Rock is porphyritic with phenocrysts of green-tinged clay, likely pseudomorphs of feldspars. Some preserved feldspar phenocrysts are present, both K-feldspar and highly altered glomerocrysts of plagioclase. Large quartz grains (0.5 mm) are present, veined by hydrothermal magnetite. Micas also present as an alteration product. Groundmass consists of feldspars, quartz, magnetite and apatite. Altered mafic phases occur as 200 micron subhedral crystals – likely pyroxene. Magnetite is present as resorbed, fractured and embayed crystals up to 300 microns in size. Hydrothermal magnetite (<1 wt % titanium) is also present with colloform habit in vein-like geometry. Apatite is present as euhedral crystals often included or at the margin of magnetite crystals, as well as in the groundmass. In one case, apatite is present as <20 micron-sized crystals clustered at the periphery of an altered K-feldspar. Some apatites are evidently zoned in back-scattered electron images, often correlating with the presence of sieve texture and resorption. It is clear that some apatites have undergone some hydrothermal alteration in this sample – these were excluded from further study. Rutile is observed as <20 micron sized crystals in the groundmass. Veining is abundant in the sample.</p>	<p>clay</p> <p>haem</p> <p>apt</p> <p>BSE Image</p> <p>500µm</p>	<p>A</p> <p>Apatite image (BSE)</p> <p>20µm</p>

CN82	Salamanca	SiO_2 (wt %) = 70.9%	GPS coordinates = 357339, 6384670
		<p>Composition: feldspar (50%), quartz (35% - both magmatic and secondary), biotite (15%), magnetite (5%), apatite, zircon, titanite.</p> <p>Porphyritic melanocratic rock with a red tinge. Phenocrysts of feldspar up to 3 mm in size are visible in hand specimen. Within the feldspars there appears to be strong alteration and replacement. Patchy and inconsistent rimming and more pervasive K-feldspar alteration of albite are present. Sericite is present at the cores of feldspar grains. Abundant quartz veinlets are observed. Biotite is present as crystals up to 0.5 mm in size which appear highly altered and can occasionally contain apatite crystals. Magnetite is present as subhedral crystals as well as in a more interstitial form. Magnetite usually displays sieve/trellis texture and has low titanium contents (hydrothermal alteration). There is likely both igneous (but altered) and hydrothermal magnetite present. Apatite crystals are infrequent but are present in the groundmass and as inclusions in magnetite and biotite. One apatite crystal is embayed. Zircon crystals are present, typically as inclusions in biotite. Titanite was observed in one 100-micron grain included in plagioclase, looking altered at edges.</p>	
			

CN11	Los Pelambres	SiO_2 (wt %) = 56.96%	GPS coordinates = 401933, 6255896
			<p>Composition: Plagioclase (50%), clinopyroxene (35%), amphibole (5%), magnetite (10%), apatite.</p> <p>Porphyritic mesocratic rock containing feldspar phenocrysts up to 5 mm in size with a strong trachytic texture. Plagioclase crystals are Ca-rich and display some oscillatory zoning. Minor replacement of feldspars by albite in vein-like structures is observed, however there is no pervasive replacement. Euhedral clinopyroxene phenocrysts up to 1 mm are present which, in one case, contained a large (400 micron) apatite inclusion. Clinopyroxene has sometimes been largely replaced by chlorite. Hornblende crystals occur as both euhedral crystals up to 1 mm in size, as well as anhedral interstitial crystals. Magnetite is present as euhedral-subhedral crystals up to 500 microns in size. Magnetite commonly displays trellis texture with exsolution of ilmenite. Apatite is uncommon. However, the few crystals present are several hundred microns in size, commonly in the groundmass. This sample appears to have undergone some alteration as seen by chlorite alteration and magnetite exsolution.</p>
			

CN40	Los Pelambres	SiO_2 (wt %) = 64.9%	GPS coordinates = 357339, 6384670
Composition: plagioclase (20%), quartz, chlorite, epidote, magnetite, apatite, titanite.			
 <p>Mostly phaneritic, green-tinged sample in hand specimen with infrequent green, mafic phenocrysts. Phenocrysts are lozenge shaped and pseudomorphed by epidote and chlorite (most likely originally amphibole). Largest phenocryst is 5 mm. More stubby phenocrysts, which may have previously been clinopyroxene, are also observed. Plagioclase microphenocrysts are abundant but have usually been pseudomorphed by quartz and are highly altered. Magnetite crystals are common and up to 100 microns in size; they appear to be largely altered. Apatite is typically associated with either magnetite or found within the groundmass and can be up to 100 microns in size. Titanite was observed only a few times, usually within chlorite and epidote or in the groundmass. The sample shows quite pervasive propylitic alteration.</p>			
 <p>BSE Image</p>			
 <p>Apatite Image (BSE)</p>			

References not cited in main text

- Aigner-Torres, M., Blundy, J., Ulmer, P., and Pettke, T., 2007, Laser Ablation ICPMS study of trace element partitioning between plagioclase and basaltic melts: An experimental approach: Contributions to Mineralogy and Petrology, doi:10.1007/s00410-006-0168-2.
- Blundy, J.D., Robinson, J.A.C., and Wood, B.J., 1998, Heavy REE are compatible in clinopyroxene on the spinel lherzolite solidus: Earth and Planetary Science Letters, doi:10.1016/S0012-821X(98)00106-X.
- Blundy, J., and Wood, B., 1994, Prediction of crystal-melt partition coefficients from elastic moduli: Nature, doi:10.1038/372452a0.
- Blundy, J.D., and Wood, B.J., 1991, Crystal-chemical controls on the partitioning of Sr and Ba between plagioclase feldspar, silicate melts, and hydrothermal solutions: Geochimica et Cosmochimica Acta, v. 55, p. 193–209, doi:10.1016/0016-7037(91)90411-W.
- Burnham, A.D., Berry, A.J., Halse, H.R., Schofield, P.F., Cibin, G., and Mosselmans, J.F.W., 2015, The oxidation state of europium in silicate melts as a function of oxygen fugacity, composition and temperature: Chemical Geology, v. 411, p. 248–259, doi:10.1016/j.chemgeo.2015.07.002.
- Deckart, K., Godoy, E., Bertens, A., Jerez, D., and Saeed, A., 2010, Barren Miocene granitoids in the Central Andean metallogenic belt, Chile: Geochemistry and Nd-Hf and U-Pb isotope systematics: Andean Geology, v. 37, p. 1–31, doi:10.4067/S0718-71062010000100001.
- Dunn, T., and Sen, C., 1994, Mineral/matrix partition coefficients for orthopyroxene, plagioclase, and olivine in basaltic to andesitic systems: A combined analytical and experimental study: Geochimica et Cosmochimica Acta, v. 58, p. 717–733, doi:10.1016/0016-7037(94)90501-0.
- Harrison, T.M., and Watson, E.B., 1984, The behavior of apatite during crustal anatexis: Equilibrium and kinetic considerations: Geochimica et Cosmochimica Acta, v. 48, p. 1467–1477, doi:10.1016/0016-7037(84)90403-4.
- Lee, R.G., 2008, Genesis of the El Salvador porphyry copper deposit, Chile and distribution of epithermal alteration at Lassen Peak, California: Oregon State University.
- McDonough, W.F., and Sun, S., 1995, The composition of the Earth: Chemical Geology, v. 120, p. 223–253, doi:10.1016/0009-2541(94)00140-4.
- Pan, L.C., Hu, R.Z., Wang, X.S., Bi, X.W., Zhu, J.J., and Li, C., 2016, Apatite trace element and halogen compositions as petrogenetic-metallogenic indicators: Examples from four granite plutons in the Sanjiang region, SW China: Lithos, v. 254–255, p. 118–130, doi:10.1016/j.lithos.2016.03.010.
- Righter, K., Yang, S., and Humayun, M., 2016, Apatite/melt partitioning experiments reveal redox sensitivity to Cr, V, Mn, Ni, Eu, W, Th and U, *in* 47th Lunar and Planetary Science Conference, <https://www.hou.usra.edu/meetings/lpsc2016/pdf/2168.pdf>.

- Smith, D.J., 2014, Clinopyroxene precursors to amphibole sponge in arc crust: Nature Communications, v. 5, doi:10.1038/ncomms5329.
- Tang, M., Erdman, M., Eldridge, G., and Lee, C.T.A., 2018, The redox “filter” beneath magmatic orogens and the formation of continental crust: Science Advances, doi:10.1126/sciadv.aar4444.
- Wilke, M., and Behrens, H., 1999, The dependence of the partitioning of iron and europium between plagioclase and hydrous tonalitic melt on oxygen fugacity: Contributions to Mineralogy and Petrology, v. 137, p. 102–114, doi:10.1007/s004100050585.